



Influence of micro-cracking on the composite resistivity of Engineered Cementitious Composites



Ravi Ranade, Jie Zhang, Jerome P. Lynch, Victor C. Li *

Department of Civil and Environmental Engineering, University of Michigan Ann Arbor, 2350 Hayward St, Ann Arbor, MI 48109, USA

ARTICLE INFO

Article history:

Received 21 March 2013

Accepted 6 January 2014

Available online xxxx

Keywords:

Electrical properties (C)

Mechanical properties (C)

Micromechanics (C)

High-performance concrete (E)

Composite (E)

ABSTRACT

Engineered Cementitious Composites (ECCs) are structural materials known for their excellent tensile ductility and damage tolerance. Previous experimental studies have shown a strong dependence of electrical resistivity of ECC on applied mechanical tensile strain (piezoresistive behavior), which can be potentially utilized for self-sensing mechanical damage for structural health monitoring. In this paper, the influence of micro-cracks on the composite electrical response of ECC under direct tension is investigated experimentally as well as analytically. For this purpose, the electrical–mechanical properties of two ECCs with different crack patterns are compared at macro (composite) and meso (single-crack) scales. An analytical model linking single-crack electrical response and crack pattern of an ECC to its composite electrical behavior is proposed in this study, and verified for both ECCs with experimental observations. Thus, a fundamental understanding of crack patterns and their effects on piezoresistivity of ECC is developed in this study.

© 2014 Elsevier Ltd. All rights reserved.

1. Introduction

Advances in structural analysis methods over the past five decades have allowed engineers to account for numerous load combinations and limit states in structural design [1]; yet, structures are often subjected to loads that are not anticipated during design necessitating their constant evaluation during service life for ensuring safety. Such evaluation is often performed using laborious visual inspections by trained engineers at regular intervals [2]; however, the reliability of such subjective evaluation has been often questioned [3,4]. Modern day structural health monitoring (SHM) techniques [5,6] have emerged as potential improvement over visual inspections. However, most of the sensing in SHM is performed through point-based sensors capturing only local damage, and there is a risk of missing critical damage in regions not in proximity to a sensor. A cost-effective distributed sensing alternative that can sense damage everywhere in the structure is needed to mitigate the risk of sudden structural failure, which is the motivation behind the development of self-sensing structural materials.

Structural materials that are self-sensing can potentially provide an effective alternative for comprehensively monitoring structural health due to their omnipresence in a structure. The feasibility of using Engineered Cementitious Composites (ECCs) as self-sensing structural materials has been demonstrated in previous studies (reviewed below). Apart from its excellent mechanical properties as a structural material, ECC possesses a unique combination of damage tolerance and piezoresistivity that make its use as a self-sensing material possible.

ECCs are ultra-ductile fiber reinforced cement-based composites which, unlike typical fiber reinforced concretes (FRCs), have a strain hardening behavior under tension as a direct result of their micro-mechanics based design [7,8]. The tensile strain capacity (tensile ductility) of an ECC is at least 100 times [9] higher than a structural concrete. At the same time, compressive strength of ECC is similar to that of High Strength Concretes (40–70 MPa). The majority of catastrophic structural failures are tension related, and therefore, particular focus is on the tensile performance of ECC. The high tensile ductility of ECC is achieved by forming multiple micro-cracks (crack width < 100 μm), which allows the material to gradually undergo controlled damage while sustaining increasing tensile stress [10]. This is in contrast to concrete and FRCs, which rapidly lose their tensile stress capacity after a small amount of damage [11]. The damage tolerance of ECC by suppressing the sudden catastrophic failure mode facilitates the quantification of damage into discrete levels and is a required property of a self-sensing structural material.

ECC, like concrete and other cement-based materials, acts as a piezoresistive material with bulk resistivity of 10^1 – $10^5 \Omega\text{-m}$, similar to that of a semi-conductor [12,13]. The microstructure of a cured cement-based material contains microscopic pores, partially filled with unbound water and dissolved ions [14]. These ions in pore water are mobilized under an externally applied electric field to create electric current. However, connectivity between the pores is limited in ECC [15], which increases the tortuosity of current flow path. In addition, high contact impedances exist between various phases of the multi-phase microstructure of ECC. Under applied mechanical strain, spatial separation between conductive phases changes causing a change in the bulk resistivity of ECC, which makes the material piezoresistive [16]. The change in resistivity of ECC with strain is more drastic under tension,

* Corresponding author.

E-mail address: vccli@umich.edu (V.C. Li).

especially during strain hardening, as compared to compression and can be utilized to sense tension related damage.

In the last three decades, researchers worldwide have investigated the piezoresistivity of cement-based materials and its applications in investigating hydration of cement paste, transport properties of concrete, and non-destructive damage detection particularly in concrete containing carbon fibers. In the 1980s, McCarter and co-workers [17–19] pioneered the application of AC impedance spectroscopy to study the microstructure and hydration of cementitious materials. It was realized that concrete's piezoresistivity and its measurement can be correlated to a variety of transport properties of concrete. Since 1990, there has been a widespread application of this technique in a number of studies related to concrete durability and cement hydration in the presence of pozzolanic admixtures. Seminal contributions in these research areas were made by McCarter [20,21], Mason [22–25], Beaudoin [26–28], Bentz and Garboczi [29,30], and their co-workers. The use of piezoresistivity of concrete containing carbon and steel fibers and other conductive fillers to detect linear-elastic strain and onset of cracking has recently gained interest among researchers. Significant advances in this field are credited to Chung [12,14,31–33], Beaudoin [34], Banthia [35,36], Han [37], Azhari [38], and their co-workers. However, none of these studies investigated the influence of inelastic multiple micro-cracking of a strain hardening cementitious composite under direct tensile loading on the composite resistivity, which is needed for developing self-sensing, damage tolerant structural materials.

Experimental investigation of the tensile piezoresistivity of ECC was reported by Hou and Lynch [13,16,39]. It was observed that the gauge factor (relative change in resistivity per unit strain) of ECC in the strain hardening region is about 3–4 times higher than that in the elastic (pre-cracking) region due to the formation of multiple micro-cracks which cause significantly larger increase in resistivity than elastic stretching of the composite. Both DC and AC galvanostatic (constant current) methods for measuring resistivity were explored in that study, and it was recommended to use AC current with frequency of at least 1 kHz for future studies to avoid polarization effects. Lin et al. [40] experimentally investigated the use of carbon black in ECC matrix for reducing the bulk resistivity, thereby enhancing the gauge factor to improve the damage sensing performance of ECC. The aforementioned feasibility studies experimentally demonstrated the piezoresistivity of ECC; however, a more insightful approach is needed for understanding the mechanisms at smaller scales behind the composite piezoresistivity of ECC.

The primary objective of this paper is to investigate analytically, as well as experimentally, the influence of inelastic multiple micro-cracking of ECC under tensile loading on its composite resistivity. For achieving this objective, two ECCs with different material compositions and crack patterns are studied, and their electrical–mechanical properties are compared at macro (composite) and meso (single-crack) scales. Detailed crack width distribution observations of the two materials are used to quantify the crack pattern. An analytical scale-linking model, derived using Kirchhoff Voltage Law of electrical circuits [41], is proposed to predict the composite electrical responses of both ECCs based on the

observed single-crack electrical response and crack pattern of ECC. While this analytical model applies to all ECCs and other strain hardening cementitious composites, it is verified experimentally for the two ECCs studied in this paper. Details of these tasks are presented in the rest of the paper.

The inelastic multiple micro-cracking, which is at the heart of the damage tolerance of ECC under tension, is recognized as the crucial link between the material's mechanical and electrical properties in this research, as the material deforms beyond its elastic limit. While past studies on utilizing piezoresistivity of concrete and carbon fiber reinforced concrete for damage detection (to prevent damage) have focused on the linear-elastic behavior of these strain softening materials, this research focuses on the inelastic behavior of strain hardening ECC and utilizes it for damage quantification into discrete levels in terms of gauge factors at various inelastic tensile strain levels. Significant contributions of this research also include the meso-scale insights into the electrical behavior of a single micro-crack and its analytical scale-linking to the composite scale electrical behavior of ECC. The scale-linking framework developed in this research can be applied in the future for studying other properties of ECC influenced by the crack patterns, such as self-healing and transport properties. In addition, a systematic statistical approach for quantifying crack patterns in ECC is developed in this study. Overall, this research is an important step toward utilizing damage tolerant strain hardening cementitious materials, such as ECC, as self-sensing resilient structural materials.

2. Experimental investigation

2.1. Materials and mix proportions

The electrical–mechanical behaviors of two ECCs, named M45-ECC and HFA-ECC, are investigated in this study. The development of M45-ECC was first reported by Wang and Li [42]. HFA-ECC, where HFA stands for High Fly Ash content, contains higher weight of fly ash per unit composite volume as compared to M45-ECC and was first reported in the literature by Yang et al. [43]. The mix proportions of these ECCs are given in Table 1. The REC-15 PVA fiber used in both ECCs has a diameter of 39 μm , length of 12 mm, and specific gravity of 1.3. The nominal strength and elongation at break of this fiber are 1600 MPa and 7%, respectively. As a polymeric material, PVA fibers are non-conducting.

Both ECCs use cement (with water) as primary binder, while fly ash is used as a secondary binder reacting with the by-products of primary hydration. The fly ash to cement weight ratio in HFA-ECC is 2.8 compared to 1.2 in M45-ECC. The water/cementitious material (cement + fly ash) weight ratio (w/cm) in both ECCs is 0.26. Unreacted fly ash particles act as fillers in ECC supplementing the primary aggregate, which is fine silica sand with mean diameter of 110 μm . Unlike concrete, ECC does not contain coarse aggregate for enhancing fiber dispersion and limiting the matrix fracture toughness, which are desirable for achieving tensile ductility. Further details about the constituents and their micromechanics design basis can be found in literature on ECC design [7,42,43].

Table 1
Mix proportions of ECCs.

| Constituent/average property | Particle size range in μm (D_{50} in brackets) | Specific gravity | Weight per unit volume, kg/m^3 | |
|-------------------------------------|---|------------------|---|---------|
| | | | M45-ECC | HFA-ECC |
| Cement (Type I) | 5–50 (15) | 3.15 | 578 | 324 |
| Fly ash (Class F) | 5–50 (20) | 2.40 | 693 | 906 |
| Silica sand | 60–250 (110) | 2.60 | 455 | 453 |
| Tap water | – | 1 | 330 | 324 |
| HRWRA | – | 1.20 | 2.7 | 2.1 |
| REC15 PVA fiber | – | 1.30 | 26 | 26 |
| Expected density (d_e) | | | 2085 | 2035 |
| Avg. specimen density (d_{avg}) | | | 1831 | 1701 |
| d_{avg}/d_e (no units) | | | 0.88 | 0.84 |

2.2. Specimen preparation

Nine rectangular coupons of each ECC were prepared in this study. After the fresh mix was poured into the molds, it was allowed to cure for 24 h at room temperature and humidity (RTH – $23 \pm 1^\circ\text{C}$ and $20 \pm 5\%$ RH). The specimens were demolded after this and stored at RTH until the age of 28 days, when they were tested.

The exterior dimensions of all rectangular coupon specimens are $254\text{ mm} \times 76\text{ mm} \times 12.7\text{ mm}$ ($10\text{ in} \times 3\text{ in} \times 0.5\text{ in}$). One of the prepared rectangular specimens is shown in Fig. 1(a). Thin aluminum plates of size $51\text{ mm} \times 76\text{ mm}$ ($2\text{ in} \times 3\text{ in}$) were epoxied to the ends of all coupons to minimize possible stress concentrations due to gripping fixtures of the tensile test system. Copper tapes, to serve as electrodes for electrical measurements, were glued using silver conductive paste on the specimens 12.7 mm (0.5 in) inwards from the edge of the aluminum plates [Fig. 1(a)] at both ends of the coupons. In addition, line markings were made 12.7 mm inwards from these copper tapes for attaching LVDTs. Four out of the nine coupons of each ECC were prepared in this manner for measuring composite properties through uniaxial tension tests.

The remaining five coupons of each ECC were notched along their centerline perpendicular to the loading axis for single-crack tests, as shown in Fig. 1(b). Such specimen preparation is similar to that in Paegle and Fischer [44]. The notch width is about $600\text{ }\mu\text{m}$ running continuously all around the specimen with depths of 15 mm on the lateral sides and 2 mm on the other two sides [Fig. 1(c)]. The notch forces the crack to occur at that section due to stress concentration and the substantially reduced cross-sectional area ensures exhaustion of the fiber

bridging capacity at stress levels lower than that required to trigger cracks in the rest of the specimen. Similar to un-notched coupons, copper tapes were glued for electrical resistance measurements across the notch as shown in Fig. 1(b).

2.3. Experiment procedures

The un-notched coupons were tested under direct uniaxial tension with fixed-fixed end grip configuration to measure the composite properties of stress-strain, resistivity-strain, and crack pattern. The test setup is shown in Fig. 2. A displacement rate of 0.5 mm/min was applied using a closed loop test system with a maximum load capacity of 100 kN . There is no set standard for testing cement-based materials under direct tension, and this displacement rate is based on the recommendations of the Japan Society Civil Engineers (JSCE) [45] for testing High Performance Fiber Reinforced Cementitious Composites (HPFRCCs). Two ultra-precision LVDTs (maximum non-linearity of $\pm 0.25\%$ full scale) were mounted at the LVDT line markers [Fig. 1(a)] parallel to the two side edges of a coupon. The engineering tensile strain in all coupons was computed by dividing the average of the two LVDT extensions by the gauge length of 102 mm (4 in), which is the distance between the LVDT line markers.

A concrete resistivity meter (Giatec RCON™ – Fig. 2) was used in this study to measure impedance between the two copper tape electrodes glued on the coupons. A constant AC current with amplitude of $4\text{ }\mu\text{A}$ and frequency of 1 kHz was applied across the two copper tape electrodes, and the voltage produced across the same electrodes was measured (two-point probe setup) every 5 s . Impedance across the

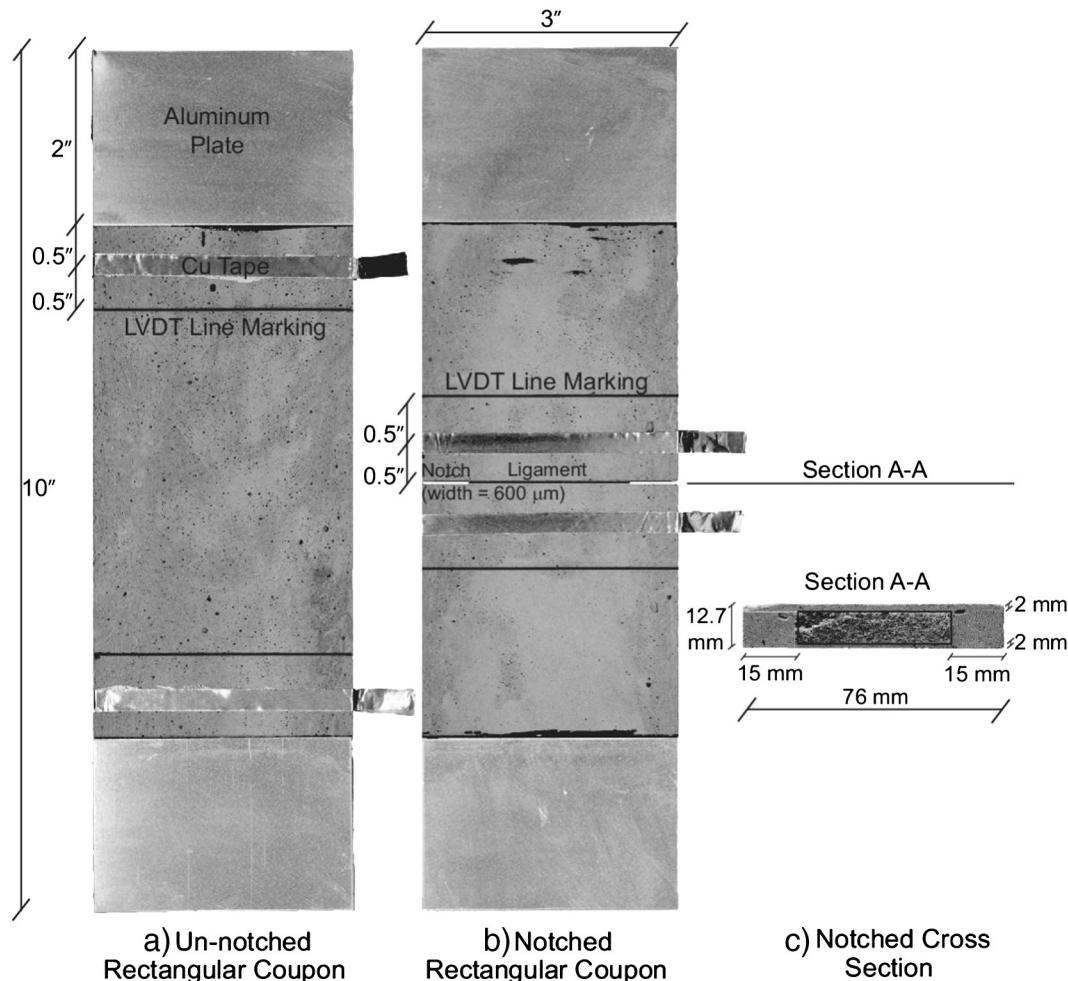


Fig. 1. Specimens for direct tension tests. [1" (inch) = 25.4 mm].



Fig. 2. Direct tension test setup.

copper tape electrodes was computed by the resistivity meter as a complex ratio of voltage and current. The phase angle of the measured impedance of ECC is always less than 15° , and therefore, resistance is approximated equal to impedance [as $\cos(15^\circ) = 0.97 \approx 1$]. Strain dependent resistivity of ECC, $\rho(\varepsilon)$, is computed from the measured resistance (R) using Eq. (1), where A is the cross sectional area of the coupon ($12.7 \text{ mm} \times 76 \text{ mm}$) and L is the distance between the two copper tape electrodes (127 mm). Bulk resistivity at zero strain (ρ_0) for each coupon is subtracted from $\rho(\varepsilon)$ to yield a change in resistivity, $\Delta\rho(\varepsilon)$. As ρ_0 of various coupons of the same ECC varies, $\Delta\rho$ is normalized by ρ_0 to compute relative change in resistivity, $\Delta\rho/\rho_0$, which is reported in the results. Gauge factor (GF) defined in Eq. (2) is used to characterize the piezoresistivity of ECC in this study.

$$\rho = \frac{R \cdot A}{L} \quad (1)$$

$$GF = \frac{\Delta\rho/\rho_0}{\Delta\varepsilon} \quad (2)$$

High resolution (0.1 pixels/ μm) pictures of the coupons during the tensile test were taken every 15 s with a high resolution digital camera. These pictures were digitally processed using ImageJ software of the National Institute of Health (NIH) to yield the variation of crack pattern (crack width distribution and number of cracks) in coupons with strain.

The procedure for testing the notched coupons to determine single-crack behavior is the same as that for un-notched coupons described above. However, the location of the copper tapes and LVDT attachment is different from the un-notched coupons (Fig. 1). Change in resistance across the crack of a unit area of the notched cross section is reported in the results.

3. Experimental results and discussion

3.1. Composite Behavior

The observed mechanical and electrical behaviors of both ECCs are plotted against tensile strain in Fig. 3. In each figure, a solid curve represents the tensile stress (σ) of a coupon specimen, and the dashed curve of the same color represents the corresponding relative change in electrical resistivity ($\Delta\rho/\rho_0$) of the same specimen. Significant mechanical

and electrical properties deduced from these figures for all coupon specimens of both ECCs are summarized in Table 2; M1–4 are M45-ECC specimens, and H1–4 are HFA-ECC specimens in this table.

3.1.1. Mechanical behavior

The mechanical stress–strain behaviors of both materials are typical of ECCs. As the coupon specimens are deformed under direct tension, average tensile stress in the specimens increases almost linear-elastically from zero. Simultaneously, local stress concentrations are created within the material microstructure near pre-existing flaws, such as air bubbles, and other micro-scale heterogeneities. This leads to the initiation and steady-state propagation of the first micro-crack in ECC matrix, and the average tensile stress in the specimen at this point is called the first crack strength (σ_{fc} in Table 2). The micromechanics based design of ECC ensures that the load at a cracked section of the specimen is safely transferred from the matrix to the bridging PVA fibers without failure of the composite. As the tensile displacement is further increased, the tensile stress rises again as the fibers are more strongly engaged by the matrix at their interface. This increase in tensile stress continues until another micro-crack is initiated at a new stress concentration site, and the cracking process described above is repeated. Ultimately, after formation of numerous micro-cracks at increasing tensile stress, the bridging capacity of the PVA fibers at one of these cracked sections is exceeded causing failure of the specimen. The multiple-cracking feature demonstrated by both ECCs is central for achieving tensile ductility and damage tolerance.

Among the two materials, HFA-ECC shows higher average tensile ductility of 4.5% compared to 2.1% of M45-ECC. The tensile strain capacity of ECC is dependent on the degree of saturation of micro-cracking, which is further dependent on the flaw size distribution, matrix fracture toughness, and fiber bridging capacity. In addition to higher tensile ductility, HFA-ECC also shows lower variation in mechanical properties of its specimens than M45-ECC, which points towards greater material homogeneity in HFA-ECC processing than M45-ECC. The property variation is captured by the Coefficients of Variation (CV) summarized in Table 2. The average elastic modulus computed from the slope of stress–strain curve in the elastic region is 17 GPa for M45-ECC and 13 GPa for HFA-ECC. In spite of the lower tensile ductility and higher variation in mechanical properties, the average ultimate tensile strength (σ_{tu}) of M45-ECC is slightly higher (5.1 MPa) than that of HFA-ECC (4.5 MPa).

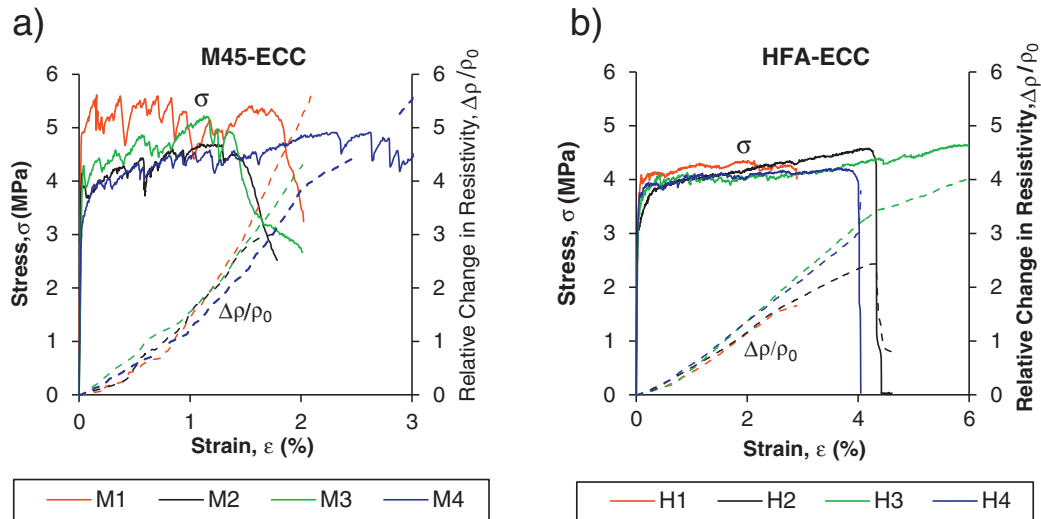


Fig. 3. Mechanical and electrical behavior of (a) M45-ECC and (b) HFA-ECC under tensile load.

3.1.2. Electrical behavior

Due to different microstructures and compositions of the two ECCs, their bulk resistivities observed at zero strain (ρ_0) are also different. The environmental conditions (temperature and humidity) also significantly influence ρ_0 , but were kept constant throughout all experiments in this study. From Table 2, it is observed that average ρ_0 for HFA-ECC (1094 Ω -m) is about 2.3 times that of M45-ECC (467 Ω -m). High (air) porosity of HFA-ECC microstructure compared to M45-ECC may be responsible for its higher bulk resistivity. The porosities of both materials are indirectly determined from the ratio of average density of cured ECC specimens (measured by weight in air and water displacement) to the expected density computed from mix proportions of individual constituent materials of ECC (Table 1). Lower density ratio in HFA-ECC indicates higher porosity than M45-ECC. Although small amounts of fly ash replacements in concrete typically reduce its porosity, large amounts of fly ash, such as that used in ECCs, cause increase in porosity [46]. In spite of the increase in porosity at high volumes of fly ash, the average pore size reduces with fly ash content [46], causing a significant decrease in transportation rate of ions [47], and therefore, higher bulk resistivity

in HFA-ECC than M45-ECC. A more thorough investigation of the material composition and microstructure is required to quantitatively explain the difference of ρ_0 between the two materials; however such investigation is beyond the scope of this paper.

Gauge factors [GF in Eq. (2)] are used to quantify the strain dependence of resistivity observed in both ECCs. Three gauge factors in three different strain regions are calculated for each coupon specimen, and an additional fourth gauge factor is calculated for HFA-ECC specimens due to their higher tensile ductility than M45-ECC specimens. The calculation of these gauge factors is shown graphically in Fig. 4 using specimen H2 of HFA-ECC as a representative specimen. GF_e is the average slope of a $\Delta\rho/\rho_0$ – ε (dotted) curve prior to cracking [Fig. 4(b)], when the mechanical behavior of the material is essentially linear-elastic. GF_{sh1} , GF_{sh2} , and GF_{sh3} [Fig. 4(a)] are the average slopes of a $\Delta\rho/\rho_0$ – ε curve after cracking as the material undergoes mechanical strain hardening (sh). Thresholds of 0.5%, 1.0%, and 2.0% are used for calculating the gauge factors during strain hardening.

The gauge factors defined above are computed for all coupon specimens and summarized in Table 2. For HFA-ECC, average GF_e is about a

Table 2

Summary of mechanical and electrical properties of ECC coupons subjected to direct tensile loading.

| Table 2(a): M45-ECC | | | | | | | | |
|---------------------|---|--|---|---|------------------------------|---|---|---|
| Spec. no. | Tensile strain capacity, ε_{tu} (%) | Ultimate tensile strength, σ_{tu} (MPa) | First crack strength, σ_{fc} (MPa) | Bulk resistivity at $\varepsilon = 0\%$, ρ_0 (Ω -m) | Elastic gauge factor, GF_e | SH ^a GF up to $\varepsilon = 0.5\%$, GF_{sh1} | SH GF for 0.5% < ε < 1%, GF_{sh2} | SH GF for 1% < ε < 2%, GF_{sh3} |
| M1 | 1.9 | 5.6 | 4.0 | 464 | 30 | 99 | 192 | |
| M2 | 1.5 | 4.7 | 3.1 | 514 | 15 | 156 | 202 | |
| M3 | 1.4 | 5.2 | 3.3 | 326 | 33 | 159 | 275 | |
| M4 | 3.5 | 4.9 | 3.1 | 565 | 17 | 122 | 258 | |
| Avg. | 2.1 | 5.1 | 3.4 | 467 | 24 | 134 | 232 | |
| SD ^b | 1.0 | 0.4 | 0.4 | 103 | 9 | 29 | 41 | |
| CV ^b | 47.0% | 8.0% | 12.9% | 21.9% | 38.2% | 21.4% | 17.7% | |
| Table 2(b): HFA-ECC | | | | | | | | |
| Spec. no. | Tensile strain capacity, ε_{tu} (%) | Ultimate tensile strength, σ_{tu} (MPa) | First crack strength, σ_{fc} (MPa) | Bulk resistivity at $\varepsilon = 0\%$, ρ_0 (Ω -m) | Elastic gauge factor, GF_e | SH ^a GF up to $\varepsilon = 0.5\%$, GF_{sh1} | SH GF for 0.5% < ε < 1%, GF_{sh2} | SH GF for 1% < ε < 2%, GF_{sh3} |
| H1 | 3.3 | 4.3 | 3.2 | 1152 | 13 | 31 | 55 | 74 |
| H2 | 4.3 | 4.6 | 2.9 | 1263 | 10 | 47 | 60 | 65 |
| H3 | 6.3 | 4.7 | 3.1 | 1003 | 11 | 32 | 72 | 91 |
| H4 | 4.0 | 4.2 | 3.1 | 957 | 16 | 40 | 75 | 81 |
| Avg. | 4.5 | 4.5 | 3.1 | 1094 | 13 | 38 | 66 | 78 |
| SD ^b | 1.3 | 0.2 | 0.1 | 140 | 3 | 8 | 10 | 11 |
| CV ^b | 28.9% | 4.4% | 4.1% | 12.8% | 21.2% | 20.0% | 14.6% | 14.1% |

^a SH stands for strain hardening.

^b SD stands for standard deviation and CV stands for coefficient of variation (SD/Avg.).

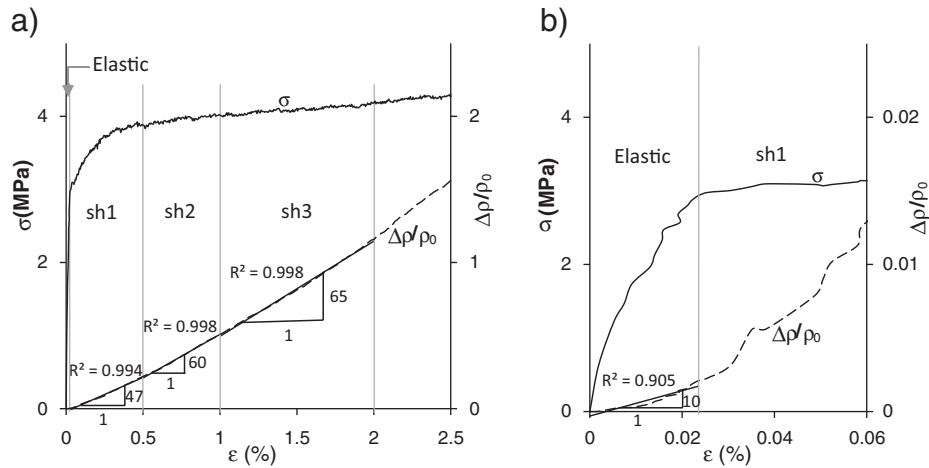


Fig. 4. Graphical representation of gauge factor calculation for specimen H2 of HFA-ECC: (a) all regions (sh: strain hardening regions) (b) zoomed elastic (pre-crack) region.

third of average GF_{sh1} and about a fifth of average GF_{sh2} . GF_{sh3} is only slightly higher than GF_{sh2} . The slope of $\Delta\rho/\rho_0 - \epsilon$ curve increases suddenly after the first crack [Fig. 4(b)], and more gradually thereafter in the strain hardening region [Fig. 4(a)]. The average GF_e of M45-ECC (24) is almost twice that of HFA-ECC (13). The change of GF from one region to another is also higher in M45-ECC as compared to HFA-ECC. For M45-ECC, the average GF_{sh1} is about 5.5 times the average GF_e , while GF_{sh2} is about 10 times the GF_e . The variation in mechanical properties noted above is reflected in the variability of gauge factors. The gauge factors of M45-ECC in all strain regions exhibit higher variability (signified by higher CV) than those of HFA-ECC. Overall, the gauge factors of both materials change with strain; however, the change in GF from one strain region to the next and the magnitudes of GF are higher in M45-ECC than in HFA-ECC.

The gauge factor [Eq. (2)] in a strain region ($\Delta\epsilon$) depends on ρ_0 and the change in resistivity ($\Delta\rho$) over $\Delta\epsilon$. The factors influencing ρ_0 are discussed above. Similar to ρ_0 , $\Delta\rho$ also depends on material microstructure and composition, which is indirectly manifested in the single-crack electrical behavior. In addition (unlike ρ_0), a significant factor influencing $\Delta\rho$ is the crack pattern (causing $\Delta\epsilon$). Both, the crack pattern and single-crack behavior, are observed for the two ECCs and their influences on the electrical behaviors of the composites are discussed below.

3.2. Crack pattern

The evolution of the crack pattern with strain in both materials was observed using photographs of coupon specimens at regular intervals during the direct tension tests. For the purpose of the following discussion, representative specimens M2 of M45-ECC and H2 of HFA-ECC are considered here. Analysis of all other specimens is performed following the same procedure and average properties are used for computations using the analytical model. Photographs of specimen M2 at 1.4% strain and specimen H2 at 4.2% strain, when both specimens achieve their respective tensile strain capacity, are shown in Fig. 5. Also shown in Fig. 5 is the central longitudinal area (dashed rectangle) of the coupons used to determine the crack widths in multiples of $10\ \mu\text{m}$ from these photographs using digital image analysis. Details of the regression analysis method, adopted for formulating a mathematical function of crack width and strain to reproduce the observed crack pattern, are presented below.

The observed crack widths from photographs are plotted for both specimens (M2 and H2) in Fig. 6. Lognormal distributions [48] best-fitting the observed crack width distributions (CWDs) are also shown in Fig. 6. It should be noted that the plotted best-fit curve is obtained by scaling up the probability density function (PDF) by the total number of cracks at a particular strain level and class interval of the histogram

($10\ \mu\text{m}$), and is, therefore, meaningful only at the crack widths which are multiples of $10\ \mu\text{m}$. However, for the analytical investigation detailed below, the actual PDF is used, which is continuous for all crack widths. Similar best-fit CWDs obtained in this manner at various strain levels are plotted in Fig. 7. For clarity of figures, the CWDs of both specimens are shown only at five strain levels in Fig. 7; however, during the direct tension test, CWDs were obtained more frequently at about 0.12% tensile strain (15 s) intervals. Further, the means (m) and standard deviations (s) of all lognormal CWDs for both specimens (M2 and H2) are plotted against strain in Fig. 8. Finally, third-order polynomials of strain best-fitting these curves are determined as shown in Fig. 8, which can be used to reproduce the lognormal distribution parameters (m and s) and, therefore, the PDF for CWD at any strain.

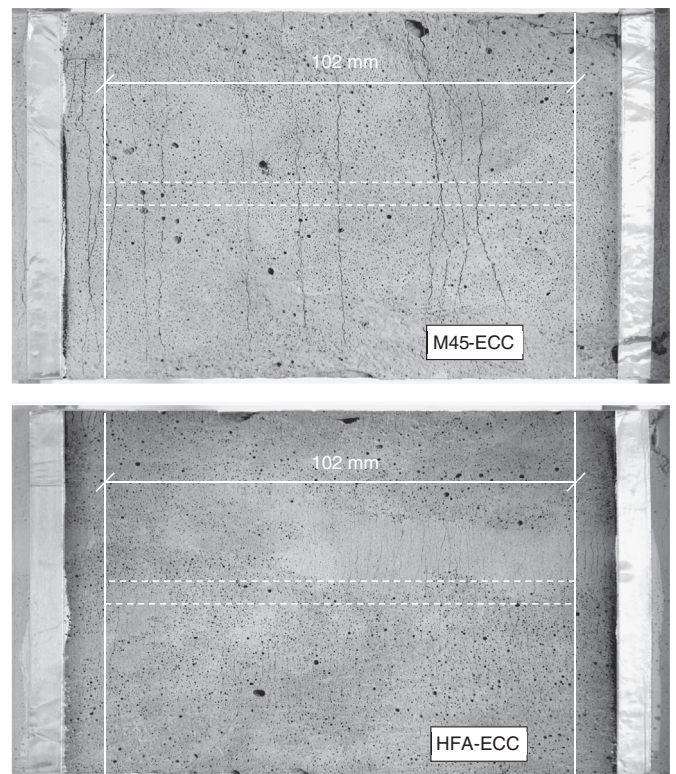


Fig. 5. Photographs of coupons showing crack patterns in specimens M2 (M45-ECC) at 1.4% strain and H2 (HFA-ECC) at 4.2% strain.

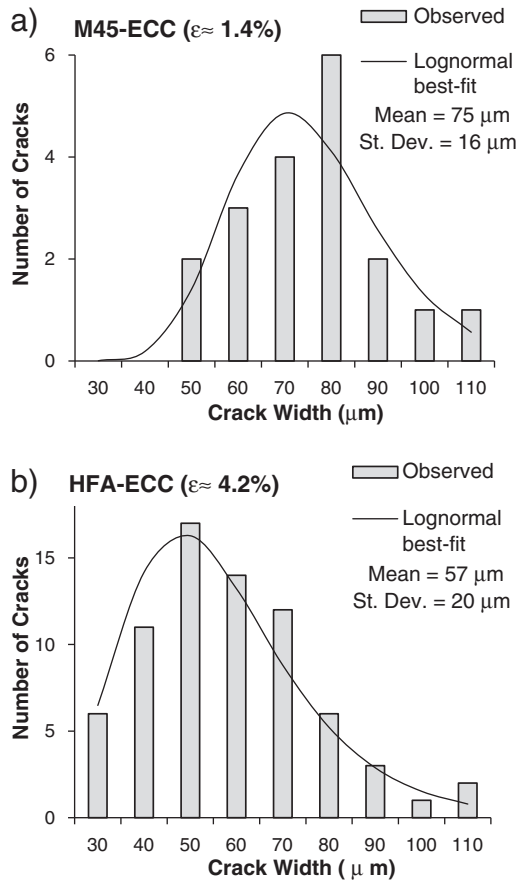


Fig. 6. Observed and best-fit crack width distributions of specimens (a) M2 (M45-ECC) and (b) H2 (HFA-ECC) at respective tensile strain capacity.

Mathematically, the lognormal PDF [49], $p(\delta, \epsilon)$ in [Eq. (3)], for CWD in a coupon specimen under direct tension is expressed as a function of crack width (δ) and parameters μ and σ , which are the mean and standard deviation, respectively, of the corresponding normal distribution. μ and σ can be further expressed in terms of mean (m) and standard deviation (s) of the lognormal distribution, which are functions of strain (ϵ) as shown in Eqs. (4) and (5). C_i and K_i ($i = 0, 1, 2, 3$) are constant coefficients determined by the regression analysis described above.

$$p(\delta, \epsilon) = \frac{1}{\delta\sigma\sqrt{2\pi}} e^{-\frac{(\ln \delta - \mu)^2}{2\sigma^2}} \quad (3)$$

$$\text{where, } \mu = \ln \frac{m^2}{\sqrt{s^2 + m^2}} \text{ \& } \sigma = \sqrt{\ln \left(\frac{s^2}{m^2} + 1 \right)} \quad (4)$$

$$m = C_3\epsilon^3 + C_2\epsilon^2 + C_1\epsilon + C_0 \text{ \& } s = K_3\epsilon^3 + K_2\epsilon^2 + K_1\epsilon + K_0 \quad (5)$$

The crack patterns in the two ECCs are very distinct. From the photographs in Fig. 5, it is apparent that the crack widths in HFA-ECC are smaller (about half) than in M45-ECC. At a given strain, the mean crack width in M45-ECC is about 1.5–2 times than that in HFA-ECC. For instance, at 1% strain, mean crack width in specimen M2 of M45-ECC is about $66 \mu\text{m}$, compared to $40 \mu\text{m}$ in specimen H2 of HFA-ECC (Fig. 8). The strain in ECC is essentially a product of mean crack width and crack number (plus a negligible magnitude of elastic strain), and as a result of smaller crack width in HFA-ECC than in M45-ECC, the number of cracks in specimen H2 is larger than in specimen M2 at any given strain (Fig. 7). Larger crack widths in M45-ECC than in HFA-ECC provide a prima-facie explanation for larger gauge factors in M45-ECC

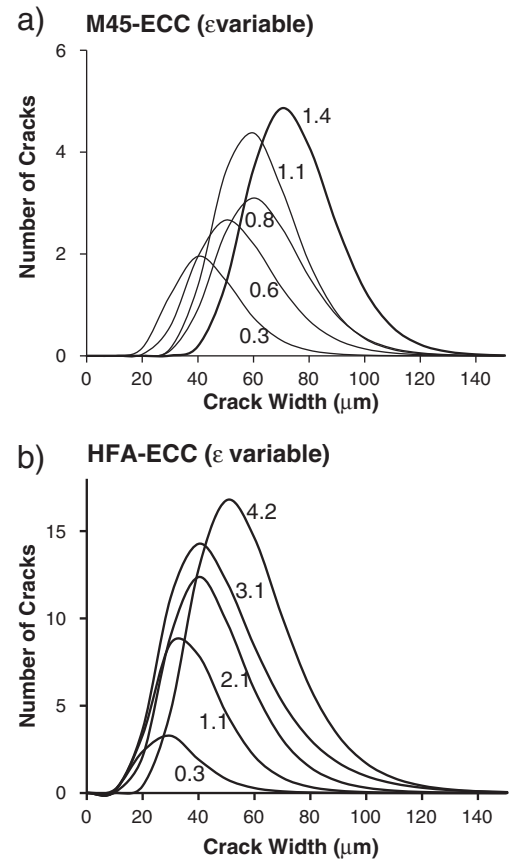


Fig. 7. Lognormal crack width distributions of specimens (a) M2 (M45-ECC) and (b) H2 (HFA-ECC) at various strain levels (numbers next to the curves denote the strain level in %).

than in HFA-ECC; however, a more insightful analysis focusing on the single-crack electrical behavior and its influence on the composite resistivity is detailed below.

3.3. Single-crack behavior

The results of single-crack tests on notched rectangular coupons (five specimens for each material) are shown in Fig. 9. The specimens (notched rectangular coupons) of M45-ECC and HFA-ECC are named MS1-5 and HS1-5, respectively. In Fig. 9, the solid curves represent the mechanical stress–crack width (σ – δ) response, and corresponding dashed curves of the same color as the solid curves represent electrical response in terms of $A \cdot \Delta R(\delta)$ (Ωm^2), which is the change in resistance [$\Delta R(\delta)$] across a unit area of notched cross-section – computed as the product of $\Delta R(\delta)$ and area (A) of the ligament [$46 \times 8.7 \text{ mm}^2$ – Fig. 1(c)]. As all micro-cracks formed during composite scale testing of both ECCs are less than $150 \mu\text{m}$, a magnified view of Fig. 9 focusing on the single-crack behavior under $150 \mu\text{m}$ is shown in Fig. 10 for discussion and analysis below. The average $A \cdot \Delta R$ – δ curves (under $150 \mu\text{m}$) for both ECCs, obtained by computing the mean of observed $A \cdot \Delta R$ values in Fig. 10 of all five notched coupons at various crack widths, are plotted in Fig. 11. Regression curves best-fitting these average curves are also shown in Fig. 11 for the purpose of utilizing them in the analytical model below.

Single-crack test results in Figs. 9 and 10 demonstrate dependence of mechanical stress and electrical resistance on tensile displacement (crack width increase). Tensile stress within a notched coupon increases linear-elastically (Fig. 10) until a crack initiates at one of the notch tips due to stress concentration. In this elastic region, which is approximately marked by a vertical dash-dot line in Fig. 10, the resistance across the

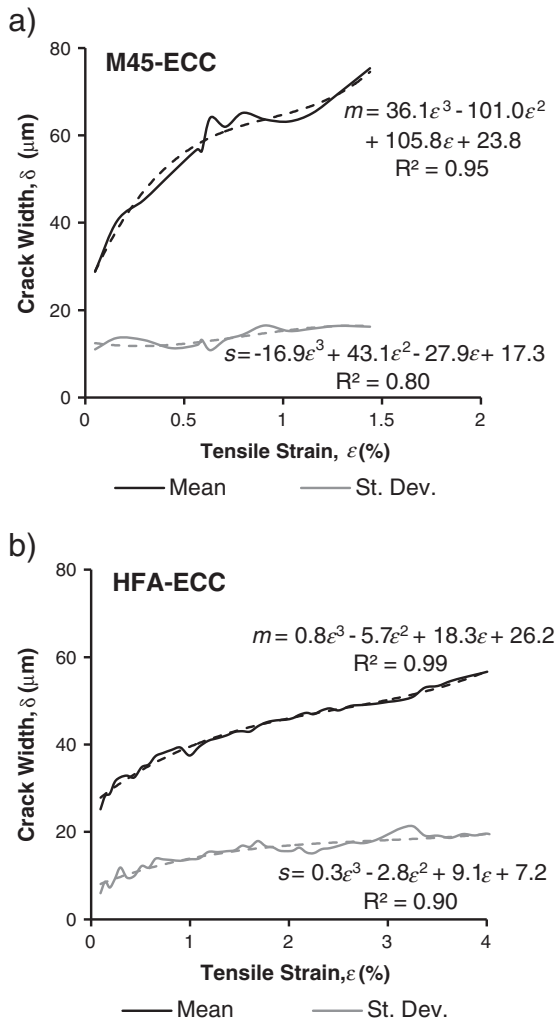


Fig. 8. Evolution of crack width distribution parameters, mean (m) and standard deviation (s), of specimens (a) M2 (M45-ECC) and (b) H2 (HFA-ECC) with strain.

notched cross-section increases gradually with a slight parabolic (concave up) trend in both materials (Fig. 11). The crack propagates throughout the matrix at the notched section under steady-state condition, similar to the un-notched coupons (described above), and the tensile stress is transferred from the matrix to the bridging fibers. After matrix cracking, while the fiber bridging stress increases with crack width more gradually than in the elastic region, the resistance across the crack increases more rapidly due to a significant increase in matrix-to-matrix contact impedance which is observable in Fig. 10 for both materials as an increase in slope of the dashed curves to the right of the vertical line.

The slope of the fiber bridging (σ - δ) curve primarily depends on the fiber/matrix bond characteristics and fiber properties [50]; however, the slope of the resistance-crack width ($A \cdot \Delta R$ - δ) curve depends prominently on the physical contact area between the two cracked matrix faces. Although the crack is “flat” locally, it undulates along the notched cross-section following the path of least resistance during propagation, as shown in Fig. 12. One of the two cracked cross-sections of each notched coupon after tensile testing is shown in this figure. A second kink (different from the elastic to post-cracking kink) in the electrical response of M45-ECC near a crack width of 50 μm is observable in Fig. 10, which is absent in the electrical behavior of HFA-ECC. This is attributable to the shallower undulations in the M45-ECC matrix crack, which lose contact after a small crack opening, unlike the HFA-ECC. The undulations on the crack surface are significantly deeper in

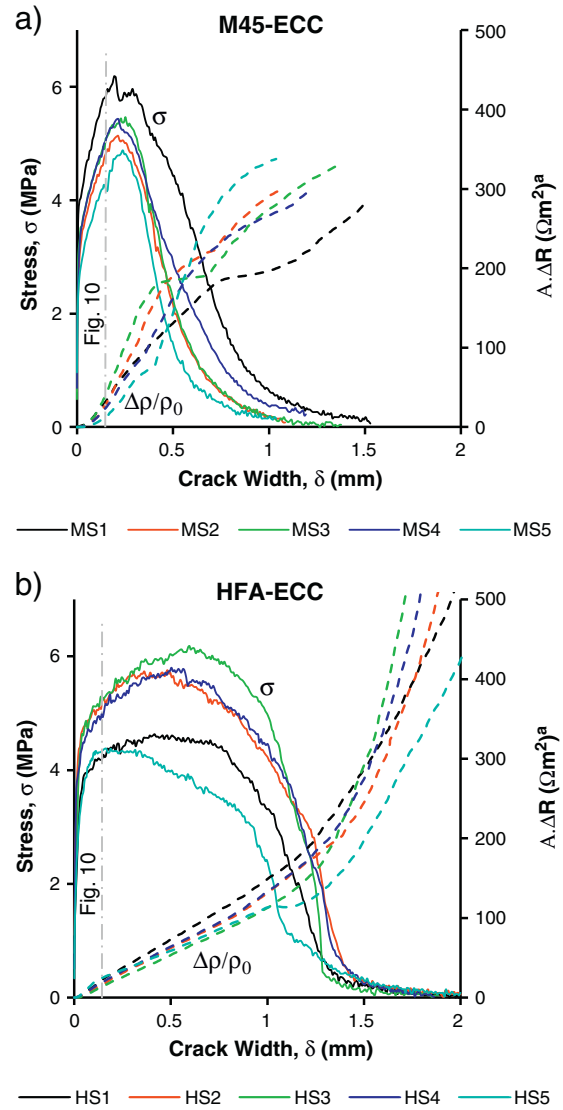


Fig. 9. Single-crack mechanical and electrical behavior of (a) M45-ECC and (b) HFA-ECC notched coupon specimens subjected to tensile load. ^a $A \cdot \Delta R$: change in resistance across a unit area of material.

HFA-ECC compared to those in M45-ECC (Fig. 12), which cause a slower rate of increase in resistance with crack width in HFA-ECC than in M45-ECC (Fig. 10).

In addition to the direct matrix-to-matrix contact conduction, the PVA fibers may also indirectly assist in conducting small fraction of electric current across the crack as long as they are effective in bridging the crack. Although PVA fibers are non-conductive, they are coated with fragments of conductive cementitious matrix which are either pulled out with the fibers or are the result of micro-spalling at the crack surface. More fibers break in M45-ECC than in HFA-ECC, which has more fibers pulling out. This can be observed in Fig. 12, which shows a lot of pulled out fibers in HFA-ECC, but not in M45-ECC, protruding from the crack surface even after complete separation of the two crack faces. Thus, breakage of fibers may contribute towards steeper rise of resistance with crack width in M45-ECC.

As the crack width is further increased beyond 150 μm (Fig. 9) through applied tensile displacement, the resistance across the crack continues to rise monotonically. Simultaneously, the fiber bridging stress increases with crack width up to its capacity and then reduces continuously until all the fibers are either pulled out or broken. Using micromechanics based analysis, [51] it can be demonstrated that the number of breaking fibers in M45-ECC plateaus when the fiber bridging

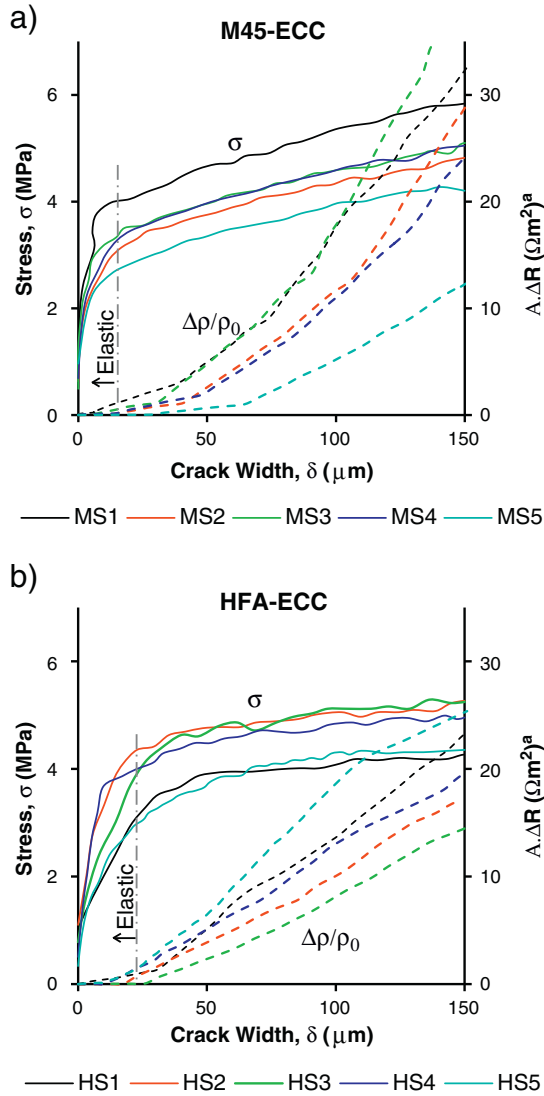


Fig. 10. Zoomed view ($\delta < 150 \mu\text{m}$) of single-crack mechanical/electrical behavior of (a) M45-ECC and (b) HFA-ECC. $A \cdot \Delta R$: change in resistance across a unit area of material.

stress is about a third of the bridging capacity in the declining branch of the σ - δ curve. This may be the reason behind a slight plateau in the $A \cdot \Delta R$ - δ curves of M45-ECC observed in Fig. 9. As most fibers in HFA-ECC pull out instead of breaking, such plateau is not observed in the steadily rising resistance of HFA-ECC. Another sharp increase in slope is observed in the electrical responses of both M45-ECC and HFA-ECC towards the end, when the fiber bridging stress is down to about 0.5–1 MPa. Micromechanical analysis [51] suggests that this region marks a complete chemical debonding (from the matrix) of the fibers with longest embedment lengths (almost half of fiber length) causing a sharp decrease in the magnitude of the declining slope of the σ - δ curves (Fig. 9), which may explain the increase in slopes of the $A \cdot \Delta R$ - δ curves thereafter. Thus, the changes in meso-scale (single-crack) electrical responses of both materials with increasing crack width are directly affected by the micro-scale interactions between fibers and matrix.

4. Analytical investigation

An analytical scale-linking model predicting the composite electrical response, based on a single-crack behavior $A \cdot \Delta R(\delta)$ and crack width distribution $p(\delta, \varepsilon)$, is derived. A coupon specimen of gauge length, L ,

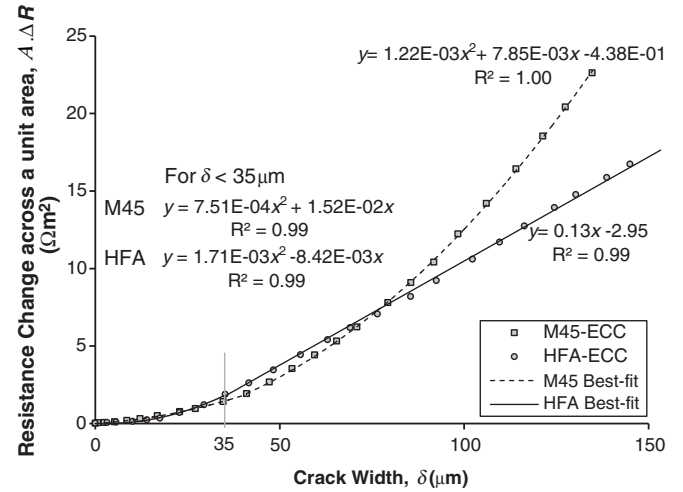


Fig. 11. Observed average and best-fit single-crack electrical behavior of M45-ECC and HFA-ECC for crack width under $150 \mu\text{m}$. (a) M45-ECC (b) HFA-ECC.

under tensile strain, ε , with multiple micro-cracks, as shown in Fig. 13, is considered for the derivation below. From the series resistor theory (a corollary of Kirchhoff Voltage Law), the resistance, $R(\varepsilon)$ in Eq. (6), across L is equal to the sum of resistance at zero strain (R_0) plus the changes in resistance, ΔR , due to very small elastic strain (ε_e) and strain due to cracking (ε_c) – note that, $\varepsilon = \varepsilon_e + \varepsilon_c \approx \varepsilon_c$ as $\varepsilon_e \ll \varepsilon_c$ (Fig. 4).

$$R(\varepsilon) = R_0 + \Delta R_e(\varepsilon_e) + \Delta R_c(\varepsilon_c) \quad (6)$$

The change in resistance due to ε_e is computed using the elastic Gauge Factor (GF_e) for the material (determined above), and the change in resistance due to ε_c is computed as the sum of increases in resistances due to individual cracks. It is assumed that there are n_i numbers of cracks with crack width δ_i and the total number of cracks ($n_1 + n_2 + \dots$) is n (Fig. 13).

$$R(\varepsilon) = R_0 + \frac{\Delta \rho(\varepsilon_e)}{\rho_0} R_0 + \sum_i n_i(\varepsilon) \Delta R_i(\delta_i) \quad (7)$$

The crack width, δ_i , can assume any real value between 0 to ∞ governed by the PDF, $p(\delta, \varepsilon)$, determined in Eqs. (3), (4), and (5) above. Thus, the number of cracks at strain ε with crack width δ_i can be expressed as Eq. (8), where $d\delta \rightarrow 0$ is a small neighborhood around δ .

$$n_i(\varepsilon) = n \cdot p(\delta, \varepsilon) d\delta \quad (8)$$

Therefore, the total resistance $R(\varepsilon)$ of the coupon can be expressed as shown in Eq. (9)

$$R(\varepsilon) = R_0 + \varepsilon_e GF_e R_0 + n \int_0^\infty p(\delta, \varepsilon) \Delta R(\delta) d\delta \quad (9)$$

The total number of cracks, n , is equal to the total tensile displacement due to cracking ($\varepsilon_c L \approx \varepsilon L$) divided by the expected value of the crack width [integral expression in the denominator of Eq. (10)]. Substituting n and rearranging the terms in Eq. (9), we get Eq. (10).

$$\frac{R(\varepsilon) - R_0}{R_0} = \varepsilon_e GF_e + \frac{1}{R_0} \left(\frac{\varepsilon L}{\int_0^\infty p(\delta, \varepsilon) \delta d\delta} \right) \int_0^\infty p(\delta, \varepsilon) \Delta R(\delta) d\delta \quad (10)$$

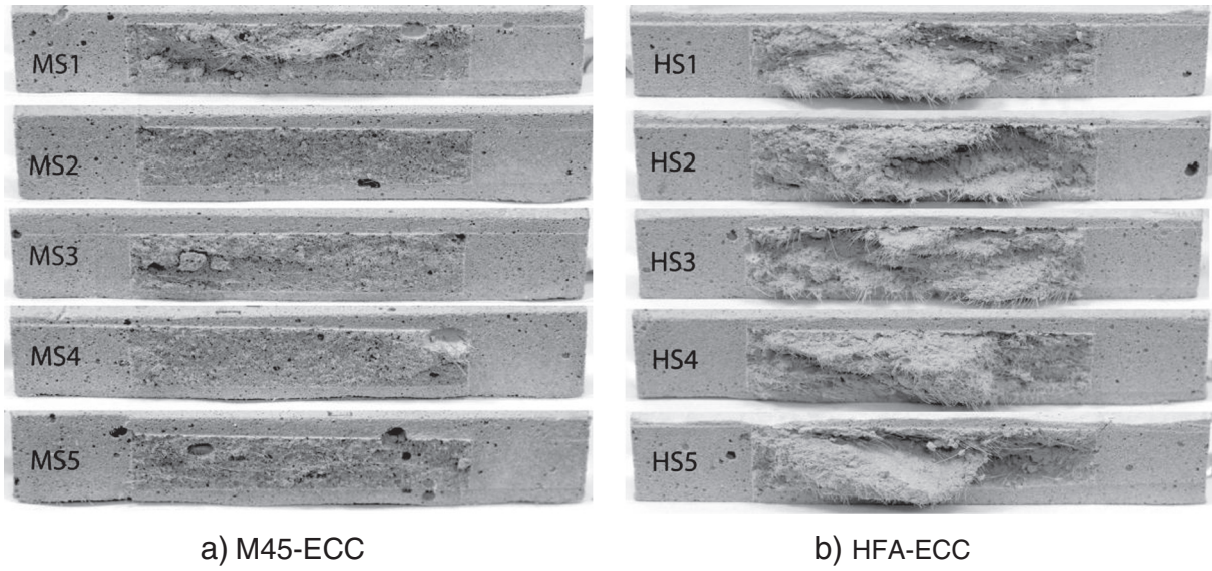


Fig. 12. Cracked cross-sections of single-crack coupon specimens of (a) M45-ECC and (b) HFA-ECC after direct tension tests.

R_0 can be expressed in terms of ρ_0 , L , and A using Eq. (1), thus obtaining Eq. (11), which is further simplified to produce the final expression of the model in Eq. (12).

$$\frac{\Delta R(\varepsilon)}{R_0} = \varepsilon_e G F_e + \frac{\varepsilon L}{\rho_0 L/A} \frac{\int_0^\infty p(\delta, \varepsilon) \Delta R(\delta) d\delta}{\int_0^\infty p(\delta, \varepsilon) \delta d\delta} \quad (11)$$

$$\Rightarrow \frac{\Delta \rho(\varepsilon)}{\rho_0} = \varepsilon_e G F_e + \frac{\varepsilon}{\rho_0} \frac{\int_0^\infty p(\delta, \varepsilon) \{A \cdot \Delta R(\delta)\} d\delta}{\int_0^\infty p(\delta, \varepsilon) \delta d\delta} \quad (12)$$

As ε_e changes very slightly after the first crack, it is assumed to be a constant equal to the strain at which the first crack occurs in both materials, which can be computed from the average first crack strength (Table 2) and elastic modulus (computed above). The assumption of constant ε_e is further justified as the increase in resistance due to elastic stretching [first term in RHS of Eq. (12)] is negligible compared to that due to cracking (second term).

5. Comparison of analytical and experimental results

Eq. (12) is numerically computed using the above determined expressions for $p(\delta, \varepsilon)$ and $A \cdot \Delta R(\delta)$ for both materials and is compared with the average of observed electrical responses (Fig. 3) of tensile coupon specimens in Fig. 14. The curves of M45-ECC (both modeled and observed) are shorter along the strain axis as M45-ECC showed lower tensile ductility (Fig. 3) than HFA-ECC. The modeled curves (solid curves) in Fig. 14 closely match the observed behaviors (dashed curves) of both materials; although, the predicted values are slightly above the observed behaviors, particularly towards higher strain levels.

A probable cause for overestimation of resistivity, as compared to the observed average response, is the fact that the analytical model does not account for variable crack width along the same crack; the model does account for variation in crack width among different cracks. While the crack width distribution, obtained through observations along the centerline of the ECC coupons (Fig. 5), captures the average width of a crack satisfactorily, it does not capture the minimum width along the crack, which may act as a short circuit reducing the resistance change across the crack. This error can be reduced by more detailed crack width observations and using a larger number of test coupons. In spite of this error, the results of the analytical model are quite close to the experimental observations, within one standard deviation of the observed average behavior.

Also shown in Fig. 14 are two dotted curves obtained by running the analytical model for two hypothetical cases examining the relative influences of single-crack behaviors and crack patterns on the electrical

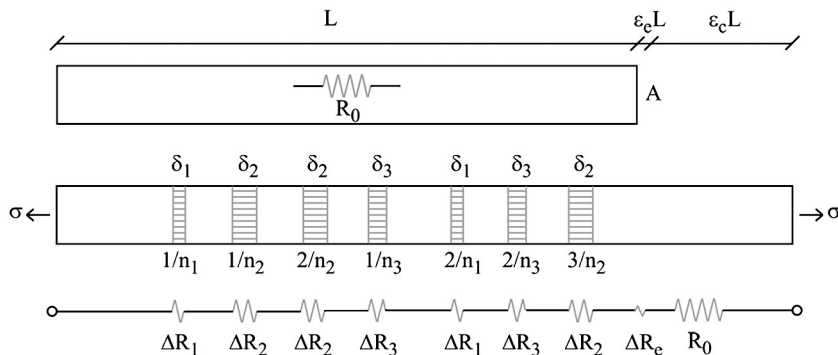


Fig. 13. Schematic representations of micro-cracking in a coupon specimen of ECC and series resistance analytical model. (Note: Figure is not to scale — size of crack widths and strain have been greatly exaggerated).

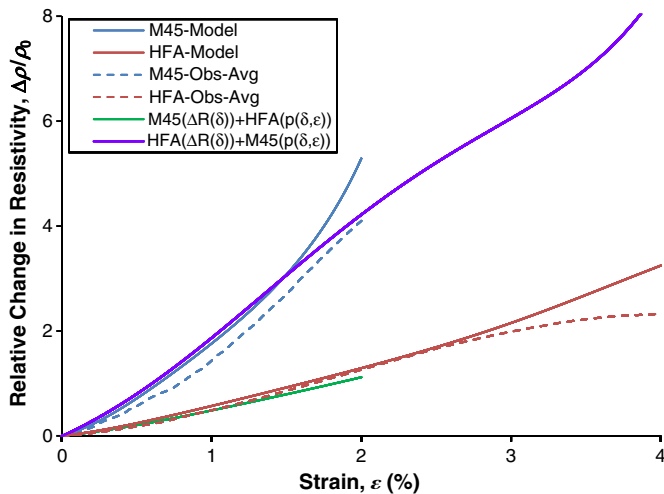


Fig. 14. Modeled versus observed average electrical response of M45-ECC and HFA-ECC coupons under direct tension.

responses of both ECCs. The curves $M45(\Delta R(\delta)) + HFA(p(\delta, \epsilon))$ and $HFA(\Delta R(\delta)) + M45(p(\delta, \epsilon))$ are obtained by using a single-crack ($A \cdot \Delta R - \delta$) behavior of one material and crack pattern $[p(\delta, \epsilon)]$ of the other (named accordingly). While the curve $M45(\Delta R(\delta)) + HFA(p(\delta, \epsilon))$ is closer to the observed response of HFA-ECC, the curve $HFA(\Delta R(\delta)) + M45(p(\delta, \epsilon))$ is closer to that of M45-ECC. This suggests that the crack width distribution has a more dominant effect on the composite electrical responses of the two materials than the single-crack behavior.

6. Summary and conclusions

This study investigated and compared, both analytically and experimentally, the influence of crack patterns on the electrical responses in terms of resistivity–strain relations (piezoresistivities) of two ECCs (M45 and HFA), which have different material compositions, mechanical behaviors, and crack patterns. The following conclusions can be drawn.

- Between the two ECCs, average tensile ductility, and therefore damage tolerance, of HFA-ECC (4.5%) is more than twice that of M45-ECC (2.1%). There is also less variability among the mechanical behavior of various HFA-ECC specimens, compared to M45-ECC specimens.
- Average bulk resistivity at zero strain of HFA-ECC (1094 $\Omega\cdot m$) is almost twice that of M45-ECC (467 $\Omega\cdot m$). The elastic gauge factor of M45-ECC is almost twice that of HFA-ECC. The strain hardening gauge factors are higher than the elastic gauge factors by about 3–6 times in HFA-ECC and by about 5–10 times in M45-ECC.
- The variability in mechanical properties of two ECCs is well reflected in the variability of their electrical properties, even in the bulk resistivities at zero strain. With more data, this can be potentially used as a non-destructive technique to establish homogeneity of material and its mechanical performance, similar to ultra-sonic resonance testing.
- Crack patterns (crack width and number) are quite different for the two materials. At any given strain, while M45-ECC has fewer cracks than HFA-ECC, the widths of cracks are larger in M45-ECC than in HFA-ECC. Among various probability density functions, lognormal distribution best-fits the observed crack patterns of both materials. A lognormal distribution has two parameters (mean and standard deviation), whose variations with strain are modeled as cubic polynomials of strain using regression analysis.
- Overall, the single-crack electrical responses are different for the two ECCs, particularly for crack widths greater than 150 μm . However, most of the cracks in both ECCs are less than 150 μm during direct

tension testing, and the average single-crack electrical responses of the two materials are only slightly different in this crack width range.

- Within a crack, matrix-to-matrix contact is important for electrical conduction, and therefore, deeper undulations of crack surface result in smaller change in resistance with increasing crack width. Effective bridging fibers coated with cementitious matrix may also indirectly assist in conducting electric current to some extent.
- Analytical model derived in this study utilizing crack pattern and single-crack behavior as inputs satisfactorily predicts the observed composite electrical response. This model is applicable for all strain hardening materials, and can be used to guide future research on the behavior and tailoring of self-sensing structural materials.
- Crack patterns (crack widths and number) have significant effect on the composite electrical behaviors of both ECCs. Larger crack widths in M45-ECC result in higher gauge factors, even though there is lesser number of cracks at a given strain in M45-ECC than in HFA-ECC. This fact is demonstrated both analytically and experimentally in this study.

Acknowledgments

The authors would like to gratefully acknowledge the U.S. Department of Commerce, National Institute of Standards and Technology (NIST)–Technology Innovation Program (TIP) for supporting this research work through Cooperative Agreement Number 70NANB9H9008. The material suppliers Lafarge, Holcim, Headwaters, US Silica, WR Grace, and Kuraray are acknowledged for providing constituent materials used in this research.

References

- [1] J.K. Wight, J.K. MacGregor, *The design process, Reinforced Concrete: Mechanics and Design*, Prentice Hall, Upper Saddle River, NJ, 2009, pp. 12–40.
- [2] FHWA, *Inspection Frequency, US Code of Federal Regulations: National Bridge Inspection Standards (Rev 2004)*, US GPO, Washington, DC, 2012, p. 267.
- [3] M.E. Moore, B.M. Phares, B.A. Graybeal, D.D. Rolander, G.A. Washer, *Reliability of Visual Inspection for Highway Bridge*, Federal Highway Administration, Washington, DC, 2001.
- [4] MnDOT, *Interstate 35W Mississippi River Bridge fact sheet*, Available online: <http://www.dot.state.mn.us/i35wbridge/pdfs/factsheet.pdf> 2007 (accessed on March 18, 2013).
- [5] J.P. Lynch, K.J. Loh, A summary review of wireless sensors and sensor networks for structural health monitoring, *Shock. Vib.* 38 (2006) 91–128.
- [6] T. Nagayama, B.F. Spencer, *Structural Health Monitoring Using Smart Sensors*, University of Illinois, Urbana-Champaign, IL, 2007.
- [7] V.C. Li, S. Wang, C. Wu, Tensile strain-hardening behavior of PVA-ECC, *ACI Mater. J.* 98 (2001) 483–492.
- [8] V.C. Li, From micromechanics to structural engineering – the design of cementitious composites for civil engineering, *J. Struct. Mech. Earthq. Eng.* 10 (1993) 37–48.
- [9] V.C. Li, On engineered cementitious composites: a review of the material and its applications, *J. Adv. Concr. Technol.* 1 (2003) 215–230.
- [10] V.C. Li, Can concrete be bendable? *Am. Sci.* 100 (2012) 484–493.
- [11] A.E. Naaman, H.W. Reinhardt, Setting the stage: toward performance-based classification, in: A.E. Naaman, H.W. Reinhardt (Eds.), *HPFRCC4, RILEM Publications S.A.R.L.*, Ann Arbor, USA, 2003, pp. 1–4.
- [12] D.D.L. Chung, Electrical conduction behavior of cement–matrix composites, *J. Mater. Eng. Perform.* 11 (2002) 194–204.
- [13] T.C. Hou, J.P. Lynch, Monitoring strain in engineered cementitious composites using wireless sensors, *International Conference on Fracture XI*, Turin, Italy, 2005.
- [14] D.D.L. Chung, Piezoresistive cement-based materials for strain sensing, *J. Intell. Mater. Syst. Struct.* 13 (2002) 599–609.
- [15] M. Sahmaran, M. Li, V.C. Li, Transport properties of engineered cementitious composites under chloride exposure, *ACI Mater. J.* 104 (2007) 604–611.
- [16] T.C. Hou, J.P. Lynch, Conductivity-based strain monitoring and damage characterization of fiber reinforced cementitious structural components, in: M. Tomizuka (Ed.), *SPIE*, vol. 5765, SPIE Press, San Diego, USA, 2005, pp. 419–429.
- [17] W.J. McCarter, M.C. Forde, H.W. Whittington, Resistivity characteristics of concrete, *Proc. Inst. Civil Eng. Pt. 2* 71 (1981) 107–117.
- [18] W.J. McCarter, A.B. Afshar, Some aspects of the electrical properties of cement paste, *J. Mater. Sci. Lett.* 3 (1984) 1083–1086.
- [19] W.J. McCarter, A.B. Afshar, A study of the early hydration of portland cement, *Proc. Inst. Civil Eng. Pt. 2* 79 (1985) 585–604.
- [20] W.J. McCarter, H. Ezirim, Monitoring the early hydration of pozzolan–Ca(OH)₂ mixtures using electrical methods, *Adv. Cem. Res.* 10 (1998) 161–168.
- [21] W.J. McCarter, H. Ezirim, AC impedance profiling within cover zone concrete: influence of water and ionic ingress, *Adv. Cem. Res.* 10 (1998) 57–66.

- [22] B.J. Christensen, T.O. Mason, H.M. Jennings, Influence of silica fume on the early hydration of portland cements using impedance spectroscopy, *J. Am. Ceram. Soc.* 75 (1992) 939–945.
- [23] B.J. Christensen, T.O. Mason, H.M. Jennings, Influence of silica fume on the early hydration of portland cements using impedance spectroscopy, *J. Am. Ceram. Soc.* 75 (1992) 939–945.
- [24] B.J. Christensen, R.T. Coverdale, R.A. Olsen, S.J. Ford, E.J. Garboczi, H.M. Jennings, T.O. Mason, Impedance spectroscopy of hydrating cement-based materials: measurement, interpretation, and applications, *J. Am. Ceram. Soc.* 77 (1994) 2789–2804.
- [25] R.A. Olson, G.M. Moss, B.J. Christensen, J.D. Shane, R.T. Coverdale, E.J. Garboczi, H.M. Jennings, T.O. Mason, Microstructure–electrical property relationships in cement-based materials, 1995, pp. 255–264.
- [26] P. Gu, P. Xie, Z. Xu, J.J. Beaudoin, A rationalized AC impedance model for microstructural characterization of hydrating cement systems, *Cem. Concr. Res.* 23 (1993) 359–367.
- [27] Z. Xu, P. Gu, P. Xie, J.J. Beaudoin, Application of AC impedance techniques in studies of porous cementitious materials I: influence of solid phase and pore solution on high frequency resistance, *Cem. Concr. Res.* 23 (1993) 531–550.
- [28] Z. Xu, P. Gu, P. Xie, J.J. Beaudoin, Application of AC impedance techniques in studies of porous cementitious materials II: relationship between ACIS behaviour and the porous structure, *Cem. Concr. Res.* 23 (1993) 853–862.
- [29] R.T. Coverdale, B.J. Christensen, H.M. Jennings, T.O. Mason, D.P. Bentz, E.J. Garboczi, Interpretation of impedance spectroscopy of cement paste via computer modelling, *J. Mater. Sci.* 30 (1995) 712–719.
- [30] B.J. Christensen, T.O. Mason, H.M. Jennings, D.P. Bentz, E.J. Garboczi, Experimental and computer simulation results for the electrical conductivity of portland cement paste, *Mater. Res. Soc. Symp. Proc.*, 245, 1991, pp. 259–264.
- [31] B. Dargos-Marian, D.D.L. Chung, G.C. Lee, Damage in carbon fiber-reinforced concrete, monitored by electrical resistance measurement, *Cem. Concr. Res.* 30 (2000) 651–659.
- [32] D.D.L. Chung, Multifunctional Cement-Based Materials, CRC Press, New York, 2003.
- [33] S. Wen, D.D.L. Chung, A comparative study of steel- and carbon-fiber cement as piezoresistive strain sensors, *Advances in Cement Research*, 2003, pp. 119–128.
- [34] P. Xie, P. Gu, J.J. Beaudoin, Electrical percolation phenomena in cement composites containing conductive fibres, *J. Mater. Sci.* 31 (1996) 4093–4097.
- [35] N. Banthia, S. Djeridane, M. Pigeon, Electrical resistivity of carbon and steel micro-fiber reinforced cements, *Cem. Concr. Res.* 22 (1992) 804–814.
- [36] R.M. Chacko, N. Banthia, A.A. Mufti, Carbon-fiber-reinforced cement-based sensors, *Can. J. Civ. Eng.* 34 (2007) 284–290.
- [37] B. Han, X. Yu, J. Ou, Multifunctional and smart carbon nanotube reinforced cement-based materials, in: K. Gopalakrishnan, B. Birgisson, P. Taylor, N. Attoh-Okine (Eds.), *Nanotechnology in Civil Infrastructure*, Springer, Berlin Heidelberg, 2011, pp. 1–47.
- [38] F. Azhari, Cement-based sensors for structural health monitoring, (MASC. Dissertation) Civil Engineering, University of British Columbia, Vancouver, Canada, 2008.
- [39] T.C. Hou, Wireless and electromechanical approaches for strain sensing and crack detection in FRC materials, (PhD Dissertation) Civil and Environmental Engineering, University of Michigan, Ann Arbor, MI, 2008.
- [40] V.W.J. Lin, M. Li, J.P. Lynch, V.C. Li, Mechanical and electrical characterization of self-sensing carbon black ECC, in: H.F. Wu (Ed.), *SPIE*, Vol. 7983, SPIE Press, San Diego, USA, 2011, pp. 16.1–16.12.
- [41] J.E. Whitehouse, Kirchhoff laws, *Circuit Analysis*, Horwood Publishing Limited, West Sussex, England, 1997.
- [42] S. Wang, V.C. Li, Engineered cementitious composites with high-volume fly ash, *ACI Mater. J.* 104 (2007) 233–241.
- [43] E.H. Yang, Y. Yang, V.C. Li, Use of high volumes of fly ash to improve ECC mechanical properties and material greenness, *ACI Mater. J.* 104 (2007) 620–628.
- [44] I. Paegle, G. Fischer, et al., Evaluation of Standardized Test Methods to Characterize Fiber Reinforced Cement Composites, in: Toledo Filho (Ed.), *SHCC2, RILEM Publications, S.A.R.L.*, Rio de Janeiro, Brazil, 2011, pp. 9–16.
- [45] JSCE Concrete Committee, et al., Recommendations for Design and Construction of High Performance Fiber Reinforced Cement Composites with Multiple Fine Cracks, in: Rokugo (Ed.), *Japan Society of Civil Engineers*, Tokyo, Japan, 2008.
- [46] C.S. Poon, L. Lam, W.Y.L., A study on high strength concrete prepared with large volumes of low calcium fly ash, *Cem. Concr. Res.* 30 (2000) 447–455.
- [47] U. Weins, W. Breit, P. Schiessl, Influence of high silica fume and high fly ash contents on alkalinity of pore solution and protection of steel against corrosion, in: V.M. Malhotra (Ed.), *5th International Conference of Fly Ash, Silica Fume, Slag, and Natural Pozzolans in Concrete*, American Concrete Institute, Milwaukee, USA, 1995.
- [48] J. Aitchison, J.A.C. Brown, *The Lognormal Distribution, with Special Reference to Its Use in Economics*, Cambridge University Press, New York, 1957.
- [49] MATLAB, Lognormal distribution, *MATLAB R2012b Documentation*, 2012.
- [50] Z. Lin, T. Kanda, V.C. Li, On interface property characterization and performance of fiber reinforced cementitious composites, *Concr. Sci. Eng. J.* 1 (1999) 173–184.
- [51] E.H. Yang, S. Wang, Y. Yang, V.C. Li, Fiber-bridging constitutive law of engineered cementitious composites, *J. Adv. Concr. Technol.* 6 (2008) 1–13.